Article

Analysis of Linear Hybrid Excited Flux Switching Machines with Low-Cost Ferrite Magnets

Muhammad Qasim [1,*] , **Faisal Khan** [1] , **Basharat Ullah** [1,*] , **Himayat Ullah Jan** [1] **and Hend I. Alkhammash** [2]

1   Department of Electrical and Computer Engineering, COMSATS University Islamabad,
    Abbottabad 22060, Pakistan; faisalkhan@cuiatd.edu.pk (F.K.); jhimayatullah@gmail.com (H.U.J.)
2   Department of Electrical Engineering, College of Engineering, Taif University, P.O. Box 11099,
    Taif 21944, Saudi Arabia; Khamash.h@tu.edu.sa
*   Correspondence: qasimrajput217@gmail.com (M.Q.); basharat.bigb@gmail.com (B.U.)

Abstract: Linear hybrid excited flux switching machines (LHEFSM) combine the features of permanent magnet flux switching machines (PMFSM) and field excited flux switching machines (FEFSM). Because of the widespread usage of rare-earth PM materials, their costs are steadily rising. This study proposes an LHEFSM, a dual stator LHEFSM (DSLHEFSM), and a dual mover LHEFSM (DMLHEFSM) to solve this issue. The employment of ferrite magnets rather than rare-earth PM in these suggested designs is significant. Compared to traditional designs, the proposed designs feature greater thrust force, power density, reduced normal force, and a 25% decrease in PM volume. A yokeless primary structure was used in a DSLHEFSM to minimize the volume of the mover, increasing the thrust force density. In DMLHELFSM, on the other hand, a yokeless secondary structure was used to lower the secondary volume and the machine's total cost. Single variable optimization was used to optimize all of the proposed designs. By completing a 3D study, the electromagnetic performances acquired from the 2D analysis were confirmed. Compared to conventional designs, the average thrust force in LHEFSM, DSLHEFSM, and DMLHEFSM was enhanced by 15%, 16.8%, and 15.6%, respectively. Overall, the presented machines had a high thrust force density, a high-power density, a high no-load electromotive force, and a low normal force, allowing them to be used in long-stroke applications.

Keywords: double stator; double mover; ferrite magnet; finite element analysis; flux regulation; linear machines

1. Introduction

The linear machine (LM) is a new type of machine directly descended from rotary machines in terms of construction [1]. The relationship between a rotary machine and the LM is sliced radially and unrolled. A linear machine can deliver direct linear thrust force without any extra mechanisms. They are reliable, fast dynamic responses, and they have a strong overload capacity due to the decrease in the mechanical conversion system.

The essential components of the LM are a mover and a stator. The secondary is ordinarily stationary, whereas the primary moves along the x-axis. The rotary machine's efficiency and power factor were significantly superior to the LM in the late 1980s. Due to the LM's robust nature, efficiency, and power factor, it has been enhanced in various ways [2]. The market and research field for the LM is regularly expanding. Magnetic levitation [3], rope tiny elevators, airplanes, shuttle launchs [4], dragging containers [5], wave energy [6], and stealth submarines [7] are some of the most common applications. In addition to converting rotational torque to linear force, LM directly transforms electrical energy to mechanical energy [8]. Various topologies have arisen due to the machine's cost and volume. The arrangement of the armature winding and PM on the mover and the construction of the secondary as a straight iron bar is thought to be a low-cost, low-volume machine. This topology, known as a Flux Switching Machine (FSM) [9], is currently being

investigated and utilized. Several types of LMs, including linear induction motors (LIM), linear synchrounous motors (LSM), stepper motors, DC motors, permanent magnet motors, and reluctance motors, have evolved and are widely used in various applications. Each motor has its own set of specs and is used for the purpose for which it was created.

For translational motion applications, linear permanent magnet synchronous motors (LPMSM), LIM, linear DC motors (LDCM), and linear switching reluctance motors (LSRM) are some suitable choices. The benefit of LPMSM is its high magnetic flux density. The LIM has a low cost but a low power factor owing to eddy losses; the LDCM requires easy speed control; and the LSRM has a robust stator structure and low construction costs but significant force ripples. The production cost of LPMSM for long-stroke applications, on the other hand, is expensive due to the higher cost of rare-earth permanent magnet materials [10].

The FSM is a new type of machine that has been discovered by researchers. Linear Flux Switching Machines (LFSMs) are commonly employed in industrial applications in the linear realm; prominent applications include railway transportation and long-stroke linear actuators [11,12]. In [13], several LFSM topologies were developed and studied based on different armature winding pattern. The machine's simple structure and sturdy character enhanced the average thrust force; the LFSM inherits superior heat management from the rotary FSM [14]. PMs and winding are placed on the short length mover to prevent using too many PMs and copper, as in traditional long-stroke applications [15–18], leading to cost savings. Electric loads are lowered due to the smaller slot area under fixed copper loss and volume due to the PM and winding allocation on the mover.

The FSM enhances efficiency and reliability [19]; to produce symmetrical magnetic flux, primary pole numbers should be in even order thrice the time, such as 6, 12, and 18 [20]. Each has its own set of advantages and disadvantages that influence the machine's performance. Different excitation techniques, such as the PMLFSM [21–23], the FELFSM [24], and the HELFSM are used to excite the FSM. The PMs are responsible for flux creation in PMLFSM, whereas the field excitation coil (FEC) winding is the source of flux in the FELFSM. In the HELFSM, both the PM and the FEC become sources of flux creation. A DC source is applied to the PM or the FEC winding to turn a machine into an electromagnet. To create flux, armature windings are energized by an AC source [25]. The FSM comprises two parts: a secondary and a mover, with the secondary containing a single iron core. The field winding and the armature winding are assigned to the mover in the FSM, whereas the iron bar is assigned to the secondary. As a result, the secondary structure of the LFSM is both stable and simple. The allocation of all active elements on the short-length mover gives the FSM a significant cost-effectiveness advantage, whilst the secondary is a bar of iron. The phrase "flux switching" describes the operation of machines in which the polarity of flux linkage changes in response to salient pole rotor motion.

The use of the PM improves flux linkages, leading to increased efficiency and maximum thrust force density. Rare-earth magnets, on the other hand, are expensive. PMLFSM topologies have been described in several places and are widely utilized in various applications [26]. The primary drawback of PMLFSM machines is that they lack flux controllability, whereas the main benefit of FELFSM machines is that they have superior flux controllability but lower force due to a weak flux linkage. Because of the quick temperature rise, the applications of PM machines are limited. PMs are replaced by DC field excitation to lower the machine's cost. Field excitation is the principal source of flux, and it eliminates the need for PMs, resulting in cost savings [11]. The HELFSM is utilized to overcome the flaws of both types of machines and achieve considerable benefits. The HELFSM machines have a high torque density and improved field weakening capabilities, allowing them to operate at a broad range of speeds [27]. The HELFSM offers flux controllability, increased efficiency, increased thrust force, and strong flux linkage. Because single-sided linear machines have a large normal force, a double-sided construction is preferred [28]. As shown in Figure 1, the LFSM is classified according to their excitation source and geometric structure [15].
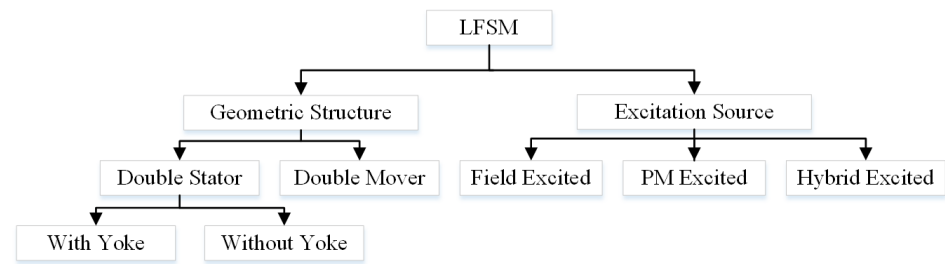
Figure 1. Classification of LFSM.

This study presents linear hybrid excited flux switching machines for long stroke applications. The proposed designs include six primary/mover slots and five secondary/stator poles. The proposed three designs, the linear hybrid excited FSM (LHEFSM), the dual stator linear hybrid excited FSM (DSLHEFSM), and the dual mover linear hybrid excited FSM (DMLHEFSM) are shown in Figure 2a–c, respectively.

(**a**)

(**b**)

(**c**)
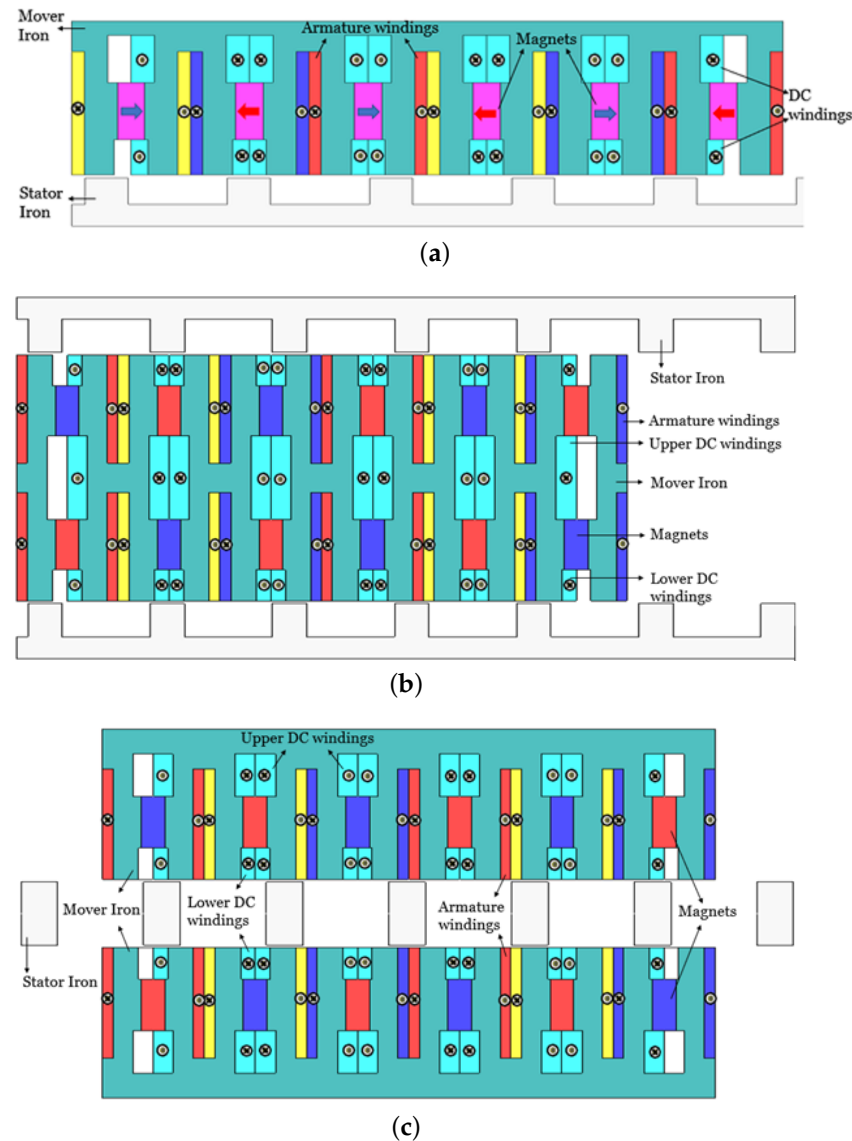
Figure 2. Proposed model (**a**) LHEFSM, (**b**) DSLHEFSM, and (**c**) DMLHEFSM.

- The primary/mover is equipped with all excitation sources (armature winding, field winding, and PM), which reduces the cost of long stator/secondary windings.
- The machine's stator is devoid of excitation sources, allowing it to be used in long-stroke applications.
- Ferrite magnets, which minimize expenses, are used. Further, its volume is reduced by 25% compared to conventional designs.
- FEC windings, which add flux regulation capability to proposed designs, are used.
- Double-sided structures are designed and investigated to solve the normal force problem that exists in single-sided structures.

2. Methodology

The JMAG-Designer software was used to create the linear machine's design. The suggested designs address the constraints of the traditional LHEFSM design. The definite formulae were used to calculate the FEC and armature coil turns. Motor materials were required to construct and demonstrate different test analyses. Initially, the design requirements, such as the size of the primary electrical machine, were identical to the traditional LHEFSM design. DC current density (Je) and AC current density (Ja) taken are 8 A/mm^2 and 18 A/mm^2, respectively. The permanent magnet (PM) of all the proposed machines was reduced in size, and excitation windings were added. The influence of some fundamental design parameters, such as split ratio, AC winding slot area, DC lower winding slot area, DC upper winding slot area, secondary tip width, and pole height, were optimized and investigated through finite element analysis in order to increase thrust density and reduce thrust ripple under load conditions.

The successful development of the primary machine designs were then evaluated and examined. The initial performances of various stator poles were researched to determine the best stator-pole combination for optimal thrust force and power performance. There were two sections to the investigation: no-load and load analysis. Characteristics of induced electromotive force (EMF), detent force, flux linkage characteristics, flux distribution, and flux lines owing to PM-FEC in the no-load investigation.

Meanwhile, for load analysis, the flux linkage at various armature current density circumstances, the maximum power and torque, the torque and the power through speed characteristics, as well as motor losses and efficiency were explored. The typical procedure of no-load and load analysis is depicted in Figure 3. The design variables of the LHEFSM, the DSLHEFSM, and the DMLHEFSM are shown in Figure 4a–c, respectively, and Table 1 enlist the proposed machine's design parameter. In FEA, the number of mesh elements and nodes in the LHEFSM were 3760 and 2160, respectively, while in the case of the DSLHEFSM and the DMLHEFSM they were 7520 and 4320, respectively.
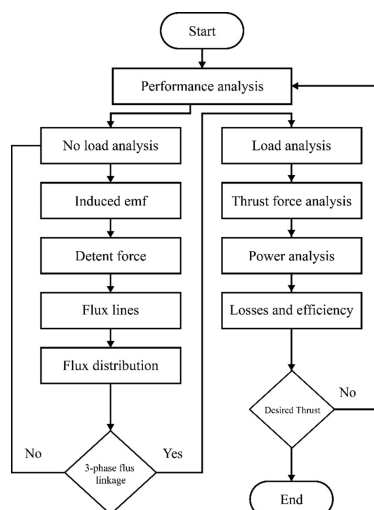
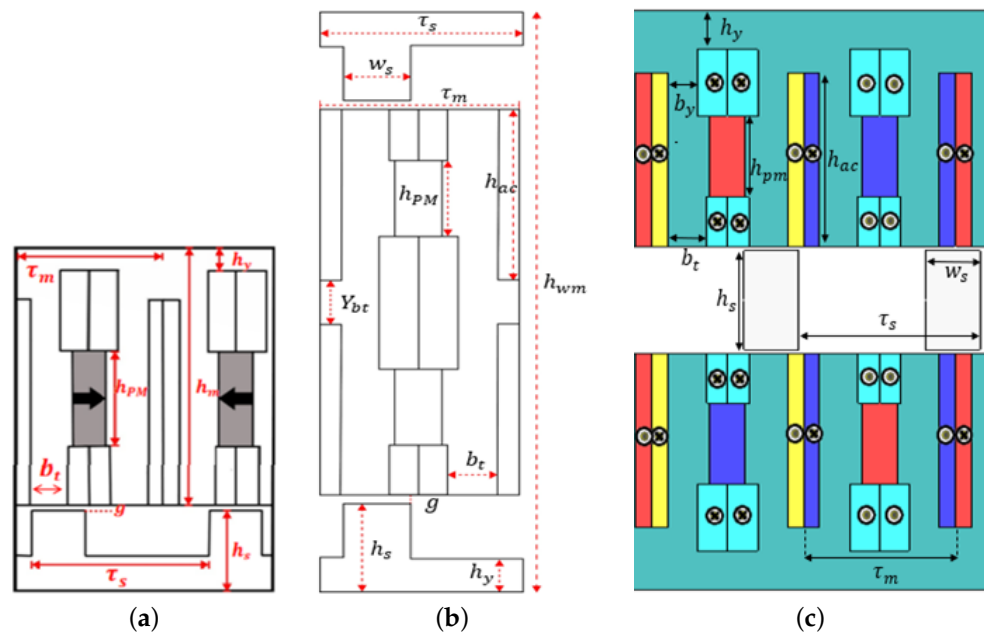**Figure 3.** Flow chart of no-load and load analysis.

Figure 4. Design variables of proposed designs (**a**) LHEFSM, (**b**) DSLHEFSM, and (**c**) DMLHEFSM.

Table 1. Parameters of the proposed designs.

Symbol	Parameter (Unit)	LHEFSM	DSLHEFSM	DMLHEFSM
τ_m	Mover pole pitch (mm)	21.832	21.832	21.832
τ_s	Stator pole pitch (mm)	26.19	26.19	26.19
h_m	Mover height (mm)	44.3	82	88.4
$h_{ac-slot}$	AC slot height (mm)	28.95	32.60	32.60
$h_{dc-upperslot}$	DC upper slot height (mm)	10.42	12.55	12.55
$h_{dc-lowerslot}$	DC lower slot height (mm)	9.264	9.264	9.264
h_{PM}	Magnet height (mm)	15.169	15.169	15.169
w_s	Stator teeth width (mm)	10.47	7.85	7.85
h_y	Mover yoke height (mm)	7	8	7.23
g	Air gap	0.8	0.8	0.8
L	Stack length (mm)	90	90	90
L_{mover}	Mover length (mm)	131	131	131
h_y	Stator height (mm)	11.58	12.50	18.55
v	Rated speed m/s	4	4	4
$N_{dc-upper}$	Upper DC coil turns	45	45	45
$N_{dc-lower}$	Lower DC coil turns	24	24	24
N_{AC}	AC coil turns	136	136	136
h_{wm}	Whole machine height (mm)	54.3	108.6	108.6

3. Working Principle

The flux path under the FEC without excitation and the field enhanced excitation is shown in Figure 5. In the absence of field excitation, a small percentage of PM flux passes through the air gap, and the majority of PM flux passes via the yoke from the N pole to the S pole, as shown in Figure 5a. This results in a shallow magnetic field flux density at the air gap without activating the excitation coil, which helps reduce iron loss and back emf throughout the high-speed performance. The magnetic flux path under the control of FEC excitation-induced magnetic field augmentation is depicted in Figure 5b. The resulting magnetic flux passes through the air gap but not through the PM, as shown by the red line in Figure 5b. In addition, the PM flux path changes from a short-circuit to a channel that spans the air gap. As a result, because the PM magnetic flux is overlaid on the magnetization formed by the FEC, the number of magnetic connections with armature increases, and the effect of magnetic field augmentation is obtained. With improved magnetic field management, high thrust is produced.
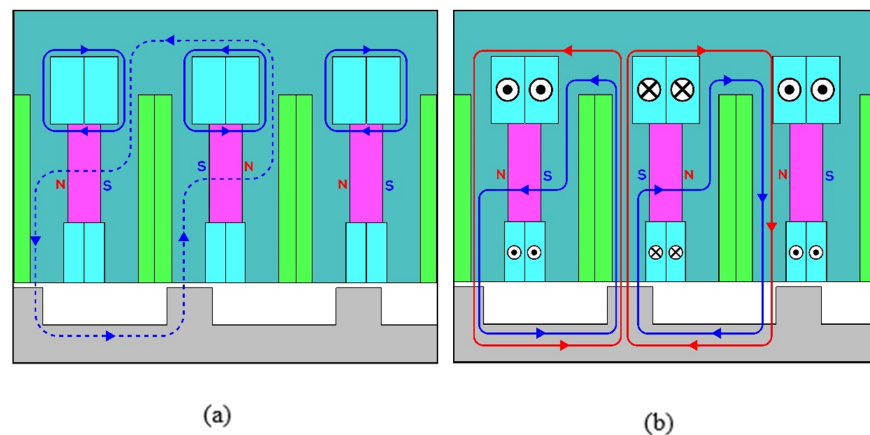

(a)   (b)

Figure 5. Operating principle (**a**) Only PM flux (**b**) PM + FE flux.

4. Analysis of the Proposed LHEFSM, DSLHEFSM, and DMLHEFSM

This section studies seven essential parameters, namely, the average value (TF_{avg}), the peak-to-peak detent force ($F_{(P-P_{Detent})}$), the peak–peak no-load flux linkage ($Flux_{(P-PPhaseB)}$), the total harmonic distortion (THD) of the B-phase, the thrust force ripple rate, the normal force ($Normal force_{(p-p)}$), and the thrust force density, which were determined. The FEA calculates the average thrust force, the peak-to-peak detent force ($F_{(P-P_{Detent})}$) and the peak–peak no-load flux linkage ($Flux_{(P-PPhaseB)}$). However, mathematical formulas were used to calculate other parameters, i.e., the total harmonic distortion (THD) of the B-phase, the thrust force ripple rate, and the thrust force density of the machine. The Fourier transform was used to obtain the THD of the B-phase ($THD_{(N,F)}$) no-load flux linkage; the formula is as follows:

$$THD_{N,F} = \frac{\sqrt{\Sigma_{m=2}^{m} Flux_m^2}}{Flux_1} \quad (1)$$

$Flux_1$ is the essential component, and $Flux_2$ to $Flux_m$ is the harmonic component. The thrust force ripple ratio was calculated by using Equation (2). Thrust force maximum and minimum values were obtained from FEA.

$$TFRR = \frac{TFR_s}{TF_{avg}} = \frac{TF_{max} - TF_{min}}{TF_{avg}} \quad (2)$$

TF_{max} and TF_{min} are the maximum and minimum thrust curves, respectively. The on-load thrust density relative to the mover volume was calculated using the following formula:

$$TFD = \frac{TF_{avg}}{V_{mover}} \tag{3}$$

Thrust force ripples are formed during the load condition counting the AC source, and the detent force is calculated at the no-load condition, that is, when the AC source is zero and other sources are active. When the AC supply is turned off, the proposed machine's detent force is detected as bipolar. The thrust profile was unipolar (desirable in this case). Positive detent force values drive the machine forward, while negative ones pull it backwards. The added stress and force can cause the thrust distribution to fluctuate.

5. Single Variable Optimization

Single variable optimization was applied to the suggested LHEFSM, DSLHEFSM, and DMLHEFSM with the yokeless secondary based on the increased average thrust force and flux strength. One type of local optimization is single variable optimization, which is also known as deterministic optimization. The goal is to optimize the flux linkage, detent force, and average thrust force, which was our main objective function (4), whereas the limits were the height/width restrictions on various machine components. Two-dimensional FEA was used to optimize many aspects of the design. The average thrust force increment determines the ideal positions until the force decreases due to core saturation. The effect of each improved parameter on the average thrust force was measured. Under constant armature copper loss, the proposed design's optimization goal was to obtain maximum output thrust force. The primary geometric parameters that impact the machine's performance were explored using optimization methods. Throughout the optimization process, τ_m, τ_s, L, g, v, J_{AC}, J_{DC}, N_{AC}, $N_{dc-upper}$, and $N_{dc-lower}$ remained constant. The flow chart of optimization is shown in Figure 6.

$$
\begin{aligned}
Objective\ Function: \quad & \max(TF_{avg}, Flux\ linkage_{p-p}) \quad and \\
& \min(Force\ Detent_{p-p}, TFRR) \\
Constraints: \quad & TF_{avg} \geq 150.7\,\text{N},\ Flux\ linkage_{p-p} \geq 0.368\ \text{Wb} \\
& Force\ Detent_{p-p} \leq 8.35\ \text{N} \quad and \quad TFRR \leq 12.9\%
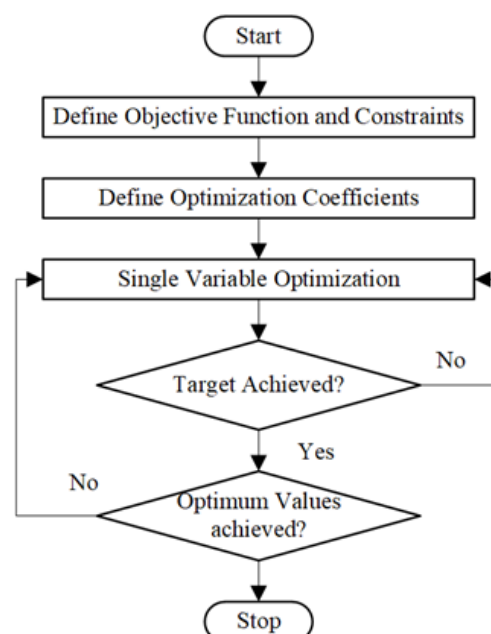\end{aligned} \tag{4}
$$

Figure 6. Optimization flowchart.

$$S.R. = \frac{h_s + g}{h_s + g + h_m} \tag{5}$$

$$S_{area,dim} = \frac{w_{slot}}{h_{slot}} \tag{6}$$

$$S_{area,dim}(dc_{lower}) = \frac{w_{slotlower}}{h_{dc-lowerslot}} \tag{7}$$

$$S_{area,dim}(dc_{upper}) = \frac{w_{slotupper}}{h_{dc-upperslot}} \tag{8}$$

$$K_{sw} = \frac{w_s}{T_s} \tag{9}$$

$$K_{sh} = \frac{h_{pole}}{h_s} \tag{10}$$

5.1. Optimization of the LHEFSM

The optimization formulae were used to optimize the nine design parameters, including h_m, $h_{ac-slot}$, $h_{dc-upperslot}$, $h_{dc-lowerslot}$, w_s, h_y, h_{pole}, h_s, and S.R. The $S_{area,dim}$, $S_{area,dim}(dc_{lower})$, and $S_{area,dim}(dc_{upper})$, which are size optimization coefficients that apply to the A.C. winding slot area, the D.C. upper winding slot area, and the lower D.C. winding slot area, respectively. The stator pole width and height optimization coefficients are K_{sw} and K_{sh}, respectively. The order of optimization coefficients, baseline values, and ranges are listed in Table 2.

Table 2. Initial values and ranges of optimization coefficients.

| Sq. No.	Coefficients	Initial Value	Ranges
1	$S.R.$	0.2279	[0.18–0.28]
2	$S_{area,dim}$	0.0897	[0.11–0.29]
3	$S_{area,dim}(dc_{lower})$	0.3366	[0.21–0.45]
4	$S_{area,dim}(dc_{upper})$	0.4987	[0.26–0.40]
5	K_{sw}	0.5	[0.25–0.65]
6	K_{sh}	0.5	[0.30–0.65]

The S.R. is the ratio of the stator height to the overall machine height, as given in Equation (5). Because material costs and thrust output are intertwined, it is critical to arriving at the optimal S.R. Figure 7a depicts the S.R. vs thrust force graph. The greatest TF_{avg} and TFD was attained by setting S.R. to 0.25. The optimal S.R. value was higher than the initial S.R., suggesting that the mover's weight and volume were lowered. As a result, the HELFSM with an S.R. of 0.25 was carefully chosen for further investigation. With a constant slot area, the armature winding slot coefficient is the ratio of the width and height of the armature slot. As a result, Equation (6) can readily find the slot's optimal width and height. The primary's tooth width and yoke height were gradually optimized by adjusting the armature winding slot coefficient. At the highest value of Equation (6), the maximum yoke height and minimum tooth width were obtained. Magnetic saturation will occur at h_y and w_{et} if the stated ratio is reduced or increased further. As shown, the greatest TF_{avg} was attained by setting the $S_{area,dim}$ ratio to 0.1411. Figure 7b depicts the thrust force variation as a function of the armature slot width.

The ratio of the width and height of a D.C. lower slot with a constant slot area is known as the D.C. lower winding slot coefficient. As a result, Equation (7) can readily find the slot's optimal width and height. The tooth width of the primary's yoke height was gradually optimized by altering the D.C. lower winding slot coefficient, as shown in Figure 7c. The maximum yoke height and the minimum tooth width were obtained at the maximum value or vice versa. The magnetic saturation at h_y and b_t will come from a

further drop or increase in the established ratio's limit. Using the $S_{area,dim}(dc_{lower})$ ratio of 0.3335, we obtained the highest TF_{avg} and TFD.

The best width and height of the slot for winding under the D.C. upper was determined using Equation (8), called the D.C. upper ratio coefficient, while maintaining the slot area constant. The set ratio's minimum value determines the maximum slot height and the minimum slot width. Changing the D.C. upper winding slot coefficient optimizes the primary's teeth width and yoke height. At the highest value of Equation (8), the maximum yoke height and the minimum tooth width were obtained. Magnetic saturation will occur at h_y and b_t if the defined ratio's limit is reduced or increased further. It was shown that picking a $S_{area,dim}(dc_{upper})$ ratio of 0.343 yields the highest TF_{avg} and TFD as shown in Figure 7d. The stator tip width was optimized using the coefficient specified in Equation (9) to obtain more sinusoidal no-load flux waveforms with lower $THD_{(N,F)}$ and maximum TF_{avg}. So, we could obtain the lowest $THD_{(N,F)}$ and the highest TF_{avg} by using K_{sw} = 0.30. Furthermore, it was demonstrated that w_s directly impacts $THD_{(N,F)}$, with lower $THD_{(N,F)}$ implying more sinusoidal waveforms and hence larger TF_{avg} and TFD. As a result, we chose HELFSM with w_s = 7.85 mm for further investigation. The ideal value was 0.30, as shown in Figure 7e. The HELFSM was developed for long-stroke applications with indefinitely long stators, as previously stated; extremely high h_{pole} optimization is required to decrease material cost and bulk. The greatest TF_{avg} was reached at a stator pole height factor (defined by Equation (10)) of 0.55 and h_{pole} = 7.02, as shown in Figure 7f. The key optimized parameter is shown in Table 3.
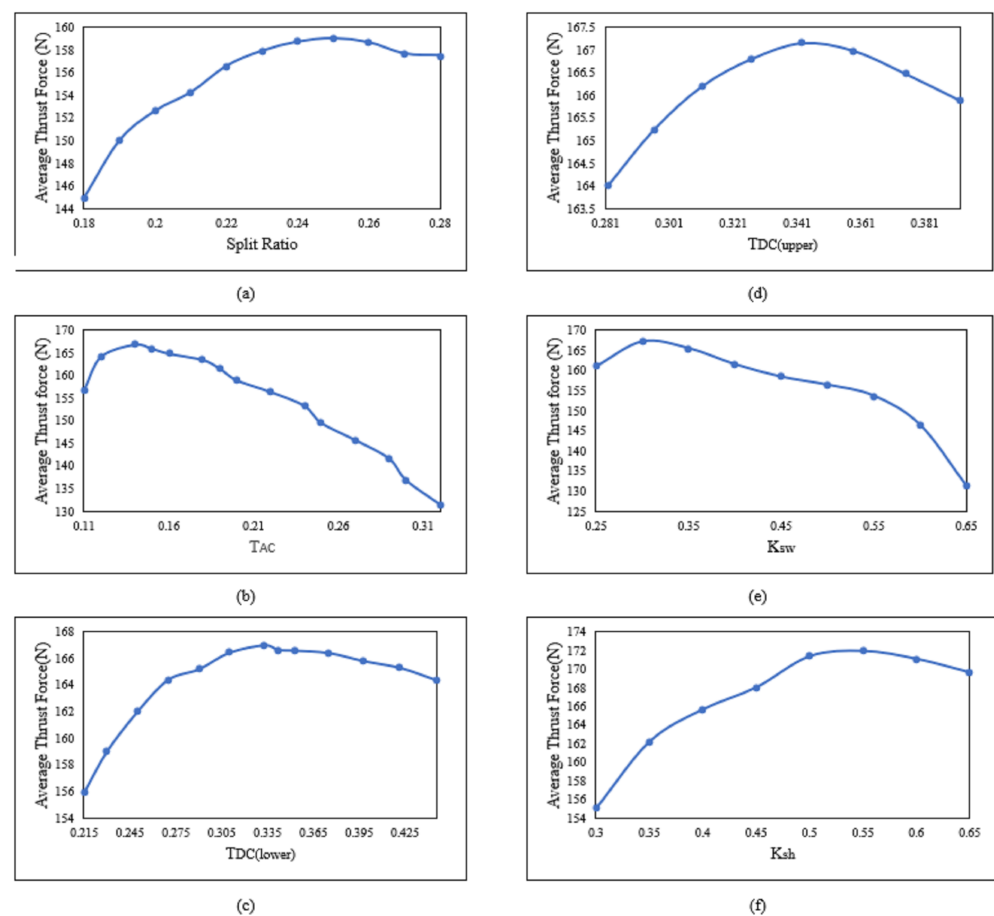
Figure 7. Optimization results of LHEFSM (**a**) split ratio (**b**) T_{AC} (**c**) $T_{DC(lower)}$ (**d**) $T_{DC(upper)}$ (**e**) K_{sw} (**f**) K_{sh}.

Table 3. Comparison of initial and optimized model.

Key Performance Indicator	Initial Values	Optimized Values
Flux linkage$_{P-P}$(Wb)	0.368	0.695
Force Detent$_{P-P}$(N)	8.35	2.76
TF_{avg}(N)	150.7	175.93
TFRR(%)	12.9	20.69

5.2. Optimization of the DSLHEFSM

The T_{AC} size optimization coefficients were used to optimize the primary pole teeth width in the AC winding slot region. The optimization coefficients for the stator pole width and the stator pole height were S_{WR} and S_{HR}, respectively. The DSLHEFSM order of the optimization coefficients, beginning values, and ranges are listed in Table 4.

$$S.R. = \frac{2h_s + 2g}{2h_s + 2g + h_m} \tag{11}$$

$$T_{AC} = \frac{w_{slot}}{h_{slot}} \tag{12}$$

$$S_{WR} = \frac{w_s}{\tau_s} \tag{13}$$

$$S_{HR} = \frac{h_{pole}}{h_s} \tag{14}$$

Table 4. Initial values and ranges of optimization coefficients of DSLHEFSM.

Sq. No.	Coefficients	Initial Value	Ranges
1	*S.R.*	0.25	[0.15–0.30]
2	*T_{AC}*	0.07	[0.07–0.28]
3	*S_{WR}*	0.3	[0.128–0.681]
4	*S_{HR}*	0.5	[0.061–0.48]

The S.R. is the ratio of the stator height to the overall machine height, as given in Equation (11). Because material costs and thrust production are intertwined, it is critical to arrive at the optimal S.R. Figure 8a depicts the S.R. vs thrust force graph. The greatest TF_{avg} and thrust force density (TFD) was reached by setting S.R. to 0.30. The optimal S.R. value was larger than the original S.R. value, suggesting that the mover's weight and volume were lowered. As a result, the model with a S.R. of 0.30 was carefully selected for further investigation. The T_{AC} coefficient is the ratio of the armature slot's width and height when the slot area is constant. As a result, Equation (12) can readily find the slot's ideal width and height. By progressively altering the armature winding slot coefficient, the tooth width and the yoke height of the primary were optimized. At the highest value of T_{AC}, the maximum yoke height and the minimum tooth width were reached. Magnetic saturation will occur at h_y and w_{AT} if the stated ratio is reduced or increased further. It was observed that setting the T_{AC} ratio to 0.07 results in the highest TF_{avg}. Figure 8b depicts the thrust force fluctuation as a function of the T_{AC} ratio. The alignment of the stator poles with slot pitch was tested while keeping the optimal stator pole width constant. The stator tip width was improved using coefficients derived in Equation (13) to generate more sinusoidal no-load flux waveforms with reduced no-load THD and maximum TF_{avg}. So, we can attain the lowest no-load THD and the highest TF_{avg} by using S_{WR} = 0.228, as illustrated in Figure 8c. As a result, the ideal value was the DSLHEFSM with a stator pole width of 7.35 mm.

The DSLHEFSM was developed for long-stroke applications with indefinitely long stators, which necessitates exceptionally high h_{pole} optimization to save material cost and bulk. Equation (14) was used to optimize the stator pole height. The greatest TF_{avg} was attained with a stator pole height factor of 0.1647 and a hpole of 10.05 mm, as shown

in Figure 8d. A multi-objective genetic algorithm was also used to find the best current angle. The thrust force was generated by the interaction of the PM flux connection with the armature current. Figure 8e depicts the change of the average thrust force with the current angle for the suggested devices. The machine's maximum thrust force was seen at the present angle of 23 degrees. As demonstrated in Figure 8f, aligning the stator pole with the main pole resulted in a greater thrust of 2.4 mm. The initial performance index and the improved performance index of DSLHEFSM are compared in Table 5.

Table 5. Comparison of initial and optimized model of DSLHEFSM.

Key Performance Indicator	Initial Design	Optimized Design
Flux linkage$_{P-P}$(Wb)	1.36	1.37
Force Detent$_{P-P}$(N)	8.04	12.3
TF$_{avg}$(N)	354	372
Normal force$_{avg}$(N)	0.90	1.22
TFRR(%)	25.2	28.2
THD$_{N,F}$(%)	3.44	3.94
TFD (KN/m^3)	405.87	426.5
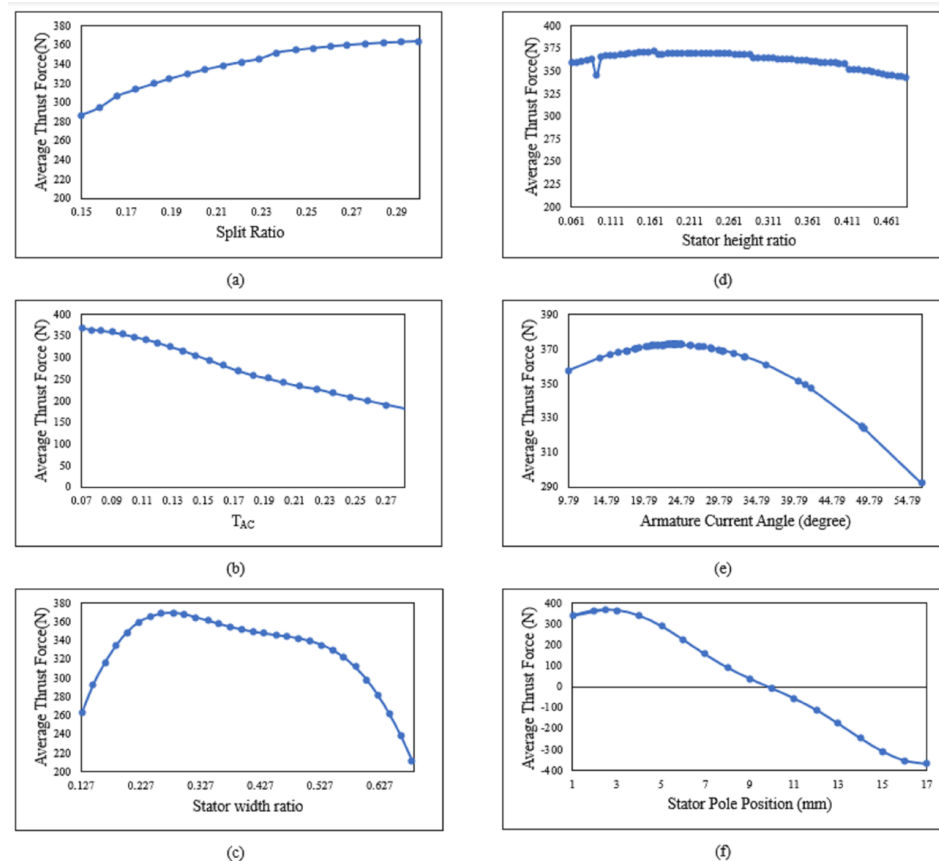
Figure 8. Optimization results of DSLHEFSM (**a**) split ratio (**b**) T_{AC} (**c**) stator width ratio (**d**) stator height ratio (**e**) armature current angle (**f**) stator pole position.

5.3. Optimization of DMLHEFSM

Table 6 shows the initial values and ranges of the DMLHEFSM parameters. S.R. in the double-sided machine is the ratio of the both stator height to the overall machine height, as specified in Equation (11). It is critical to recognize that materials and thrust production cost determine the optimal S.R. A graph of S.R. vs. thrust is shown in Figure 9a. By setting S.R. to 0.185, the maximum value was achieved. The ideal value of S.R. was lower than the initial S.R., indicating that the secondary's weight and volume were reduced.

As a result, a design was carefully selected as the model with a S.R. of 0.185 for further research. The S.R. value did not fall any more when the volume of the primary grew. T_{AC} is the width-to-height ratio of an armature slot with a fixed slot area. As a result, determining the slot's optimal width and height is simple from Equation (12). By adjusting the armature winding slot factor, the primary side's tooth width and yoke height were gradually optimized. The tooth width was shortened, and the thrust was low at the minimal ratio. The tooth width was not increased any more due to the armature slot width constraint. The armature slot's winding area was kept constant. The primary tooth width should be at least 5.5 mm. Magnetic saturation occurs when the prescribed ratio is dropped further. With a T_{AC} ratio of 0.0705, the highest TF_{avg} was attained. The T_{AC} ratio graph depicts the thrust change in Figure 9b. The stated coefficients optimize the secondary pole width to produce more sinusoidal unloaded flux waveforms with reduced THD and maximum TF_{avg} in Equation (13). Figure 9c shows that setting $S_w = 0.299$ results in a minimal no-load THD and a maximum TF_{avg}. As a result, DMLHEFSM with a secondary pole width of 7.85 mm is the best option. DMLHEFSM is designed for long-stroke applications with an infinitely long secondary pole h_{pole}, as previously indicated, and optimization is required to reduce material costs and volume. To optimize the height of the secondary poles, use Equation (14). The results in Figure 9d demonstrate that the greatest TF_{avg} was attained when the high secondary coefficient was 1. The secondary yoke was eliminated during secondary height optimization, resulting in a secondary height of 18.55 mm. Additional analysis was performed on the segmented secondary. Table 7 shows the performance indicator of the optimized design.

Table 6. Initial values and ranges of optimization coefficients of DMLHEFSM.

Sq. No.	Coefficients	Initial Value	Ranges
1	S.R.	0.25	[0.185–0.30]
2	T_{AC}	0.07	[0.07–0.10]
3	S_w	0.31	[0.10–0.65]
4	S_h	0.75	[0.32–1.0]
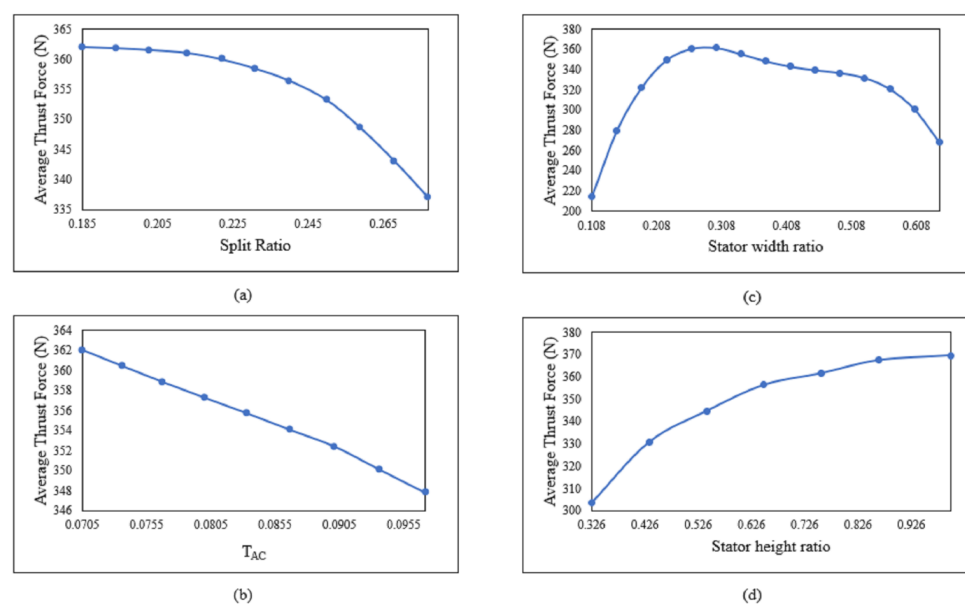
Figure 9. Optimization results of DMLHEFSM (**a**) split ratio (**b**) T_{AC} (**c**) stator width ratio (**d**) stator height ratio.

**Table 7.** Initial and optimized performance index.

Key Performance Indicator (Unit)	Initial Design	Optimized Design
$Flux\ linkage_{P-P}(\text{Wb})$	1.33	1.37
$ForceDetent_{P-P}(\text{N})$	6.89	6.54
$TF_{avg}(\text{N})$	353	370
$Normal\ force_{p-p}(\text{N})$	0.59	0.18
$TFRR(\%)$	21.7	26.1
$THD_{N,F}(\%)$	2.16	2.19

6. FEA Based Results

6.1. Flux Distribution

As shown in Figures 10–12 the entire model flux line distribution is determined when the model is at its initial position. Figure 10 shows the no-load and loaded flux lines of the LHEFSM, respectively. The end teeth have some magnetic flux lines that run through them. These magnetic flux leaks will harm the machine's magnetic circuit, which is known as the longitudinal end effect that is common in linear machines. The linear machine's end effect is caused by the propagating magnetic field's inability to merge with itself. It produces a nonuniform magnetic flux density dispersion along the length of the motor. By increasing the number of poles, the end effect is lessened. Figure 11 depicts the flux lines of the DSLHEFSM at the no-load and loaded conditions, respectively. In the DSLHEFSM, the yoke is removed so the flux moves between the two stators. In the DMLHEFSM, the flux moves between the yoke of both movers followed by the stator. Figure 12 shows the no-load and loaded flux lines of DMLHEFSM, respectively.

(a)   (b)
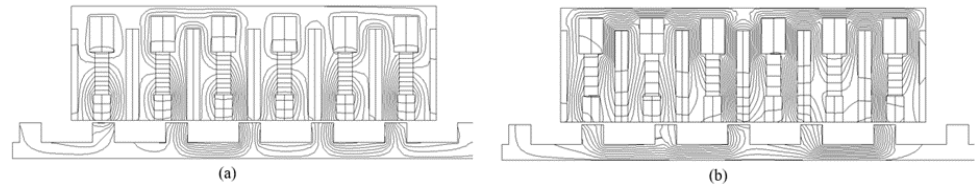
Figure 10. Flux line distribution of the LHEFSM: (**a**) no-load and (**b**) Loaded.

(a)   (b)
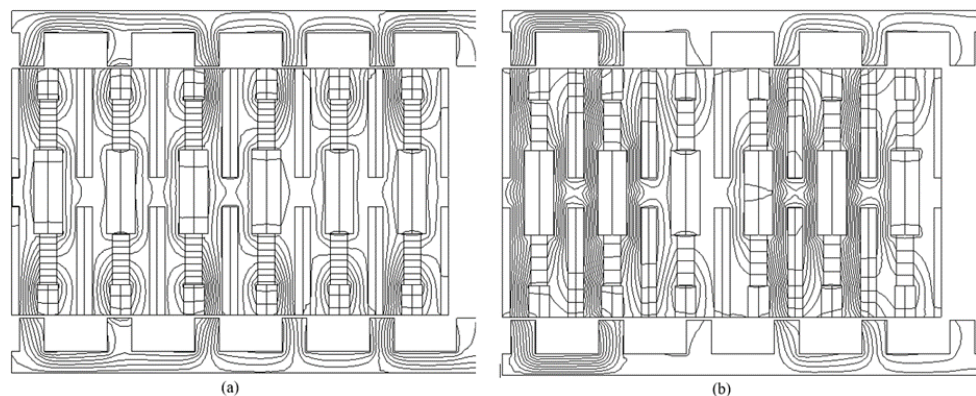
Figure 11. Flux line distribution of the DSLHEFSM: (**a**) No-load and (**b**) loaded.
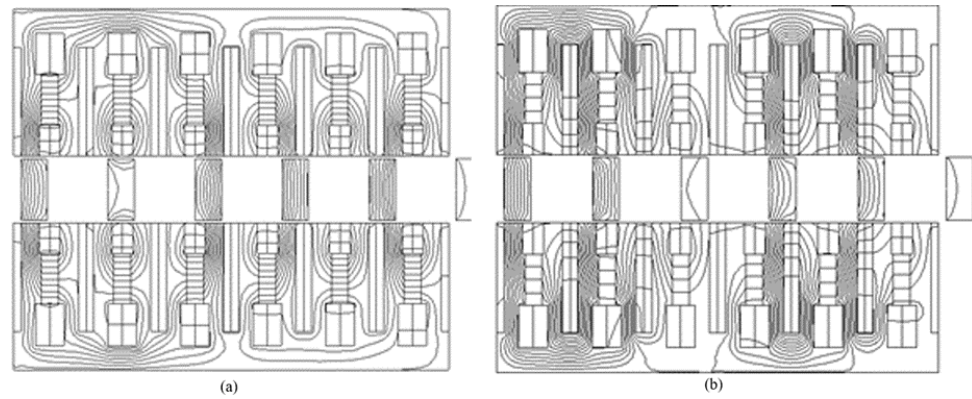
Figure 12. Flux line distribution of DMLHEFSM: (**a**) No-load and (**b**) loaded.

6.2. Flux Linkage and Back EMF of LHEFSM, DSLHEFSM, and DMLHEFSM

Flux linkage and back EMF are the two key criteria that affect the HELFSM's performance. To examine the influence of harmonics on the machine, the flux linkage and the back EMF must be determined. Figures 13–15 depicts each phase's loaded flux linkage and the accompanying harmonic waveform of all designs. As illustrated in Figures 13b–15b, the higher fifth-order components found in the flux linkage of phase A and phase B demonstrate that phase A and phase B are placed at opposite ends of the machine. Because it is placed in the machine's core, only phase C is genuinely unaffected by the longitudinal end effect. The LHEFSM is frequently conceived as an asymmetric system, yet the core components do not differ significantly between the three stages. Due to increased sources, the flux linkages of both double-sided designs achieved up to 0.6 Wb, and LHEFSM allowed 0.3 Wb. In most cases, the output thrust was proportional to the back EMF and can be found by Equation (15).

$$e = \frac{d\phi}{dt} \tag{15}$$
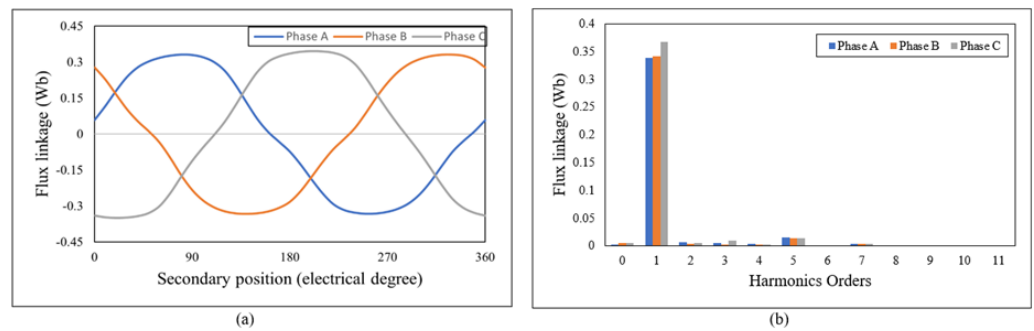
Figure 13. (**a**) Flux linkage of LHEFSM (**b**) harmonic order.
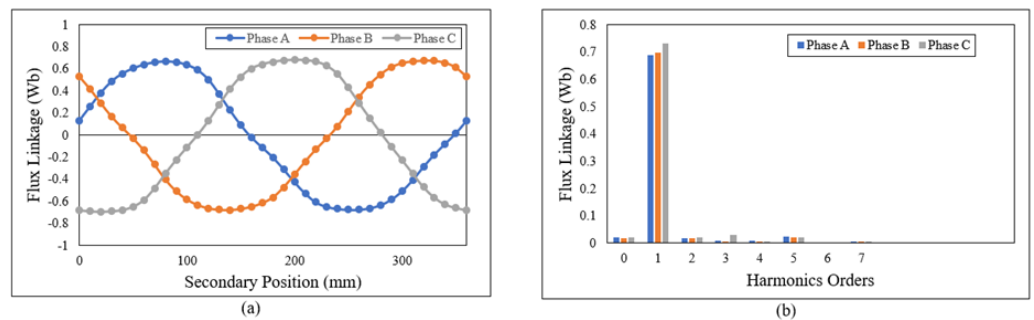
Figure 14. (**a**) Flux linkage of DSLHEFSM (**b**) harmonic order.
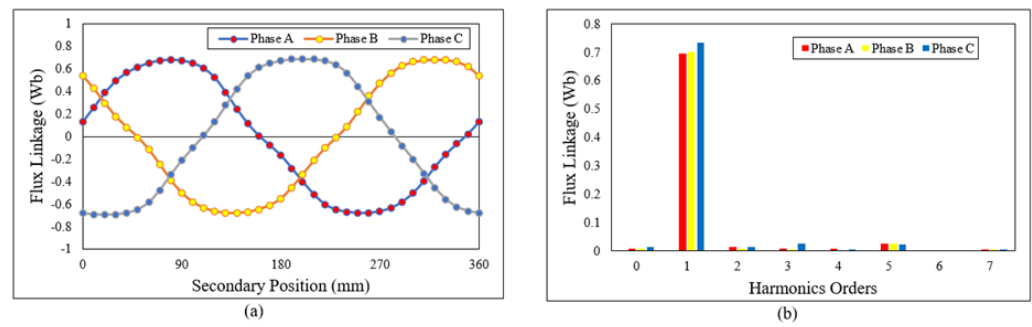
Figure 15. (**a**) Flux linkage of DMLHEFSM (**b**) harmonic order..

The back EMF of the proposed designs is illustrated in Figure 16 at a velocity of 4 m/s, where *e* and *ϕ* denote the back EMF and the flux linkage, respectively. The back EMF of LHEFSM reached up to 80 volts, and both double sided designs approached 150 volts.

(**a**)

(**b**)

(**c**)
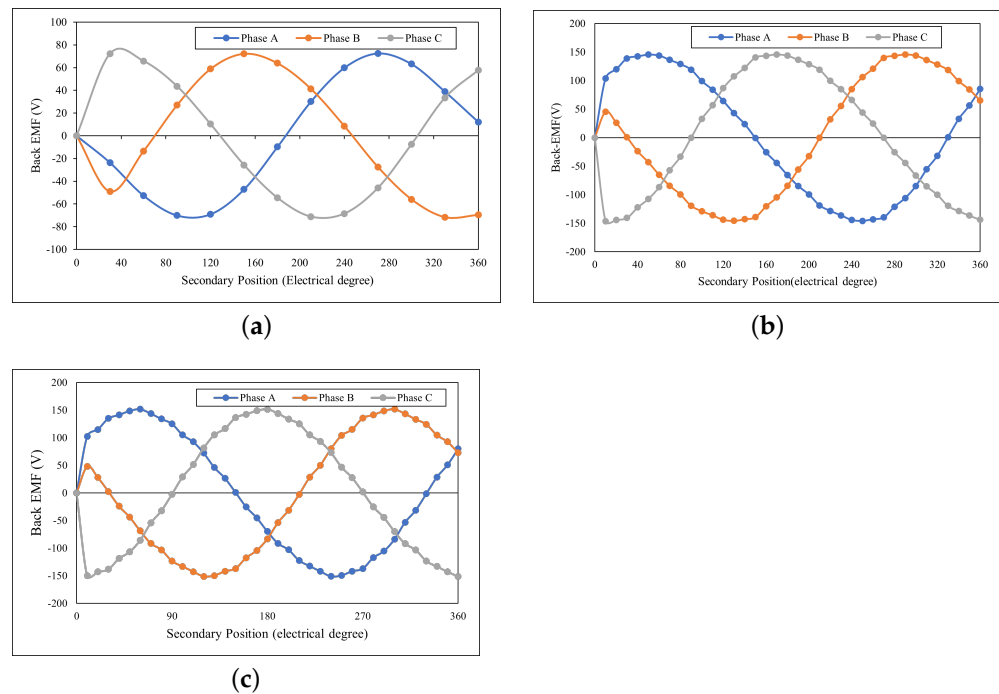
Figure 16. Back EMF (**a**) LHEFSM, (**b**) DSLHEFSM, and (**c**) DMLHEFSM.

6.3. Flux Regulation

Figure 17 depicts the proposed machine's flux boosting capabilities at various FE current densities, i.e., Je = 1 to 8 (A/mm^2). The flux density in the air gap increases as the current density alters, resulting in improved flux linkage. To summarize, the suggested LHEFSM's flux regulation capability mostly depends on the FE current, and the flux linkage is symmetrical and sinusoidal. The DSLHEFSM flux regulation characteristics were also examined with the flux linkages and the thrust force. By increasing the FEC current density from 0 to 8 (A/mm^2) in Figure 18, the regulation of the thrust force was also tested. As shown in Figure 19, the DSLHEFSM regulates when the D.C. current density was changed from −8 to +8.
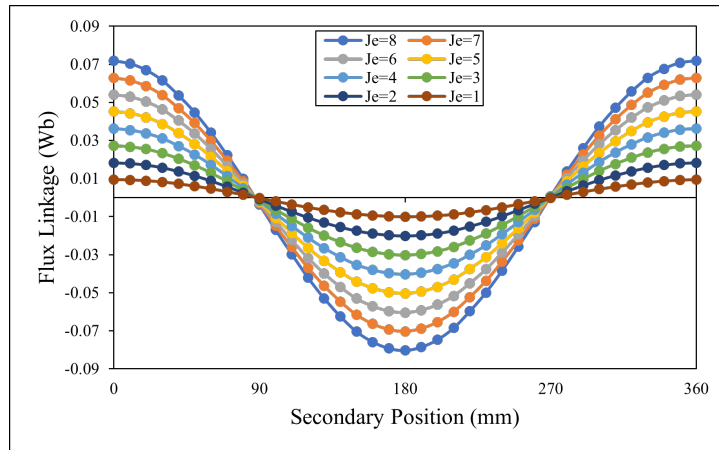
Figure 17. Flux regulation of LHEFSM.
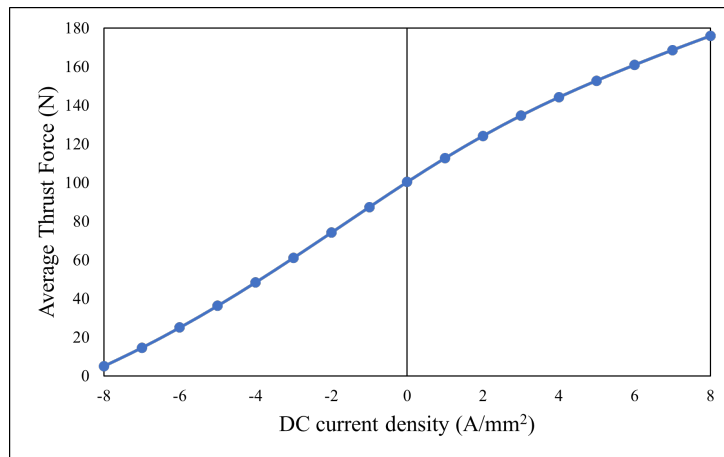
Figure 18. Flux regulation of LHEFSM with D.C. current density along thrust force.
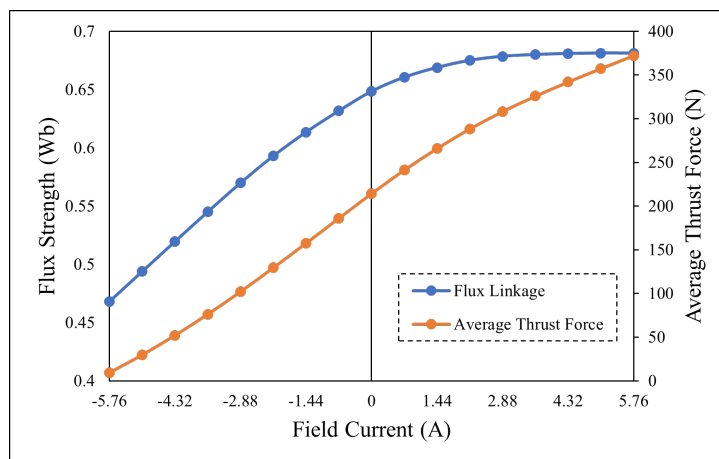
Figure 19. Flux regulation of DSLHEFSM.

6.4. Thrust Force

The results of different models' thrust forces under loads further verify the aforementioned study. As demonstrated in Figure 20, the average thrust and thrust fluctuation improved following optimization; the optimized model had a 14% increase in average thrust force. At the same current density, the thrust force in the original model was 150.7 N, increasing to 175.93 N after optimization. The proposed design achieved 15% higher thrust force compared to the conventional model [29]. The average thrust and thrust fluctuation improved after optimization, as shown in Figure 21; the optimized model had a 5% increase

in the average thrust force of both double-sided designs. After optimization, the thrust force in the DSLHEFSM improved from 353 N to 372 N, while the thrust force in the DMLHEFSM improved from 353 N to 370 N, which is 16.8% and 15.6% higher, respectively, than the conventional design thrust force [30].
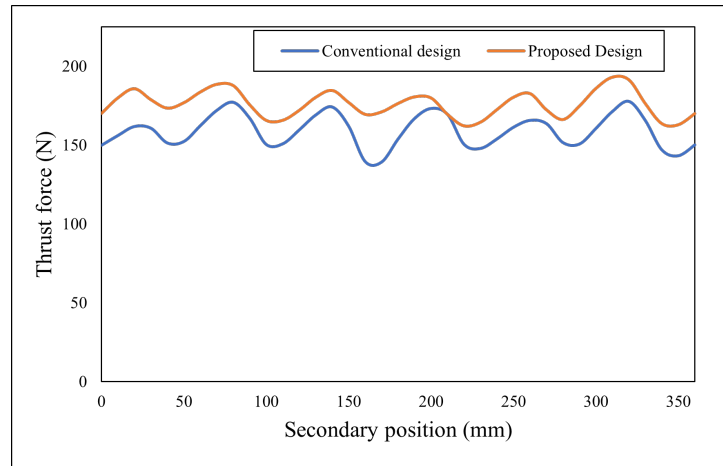
Figure 20. Thrust force characteristics of LHEFSM and conventional design.
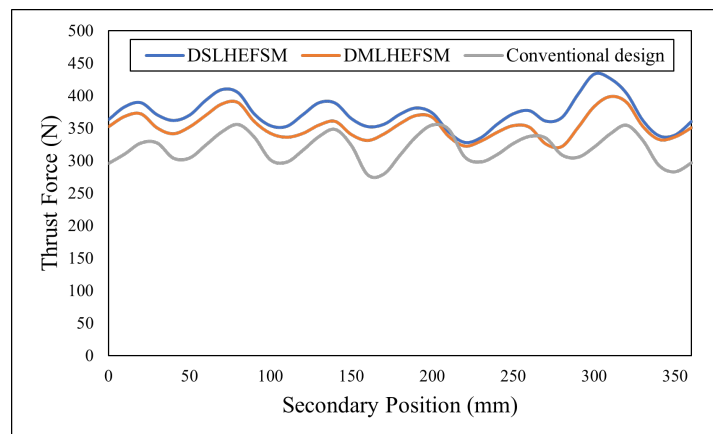
Figure 21. Thrust force of DSLHEFSM, DMLHEFSM, and conventional design.

6.5. Variation in Thrust Force as a Function of Current Density

The linear behavior of average thrust of LHEFSM is shown in Figure 22 when the armature current density was varied from 0 to 18 Amm^2. Because of flux leakage and demagnetization, the variation was linear at first but became nonlinear after reaching current density. In Figure 23, the behavior of double-sided designs was depicted in the same way as single-sided patterns are depicted.
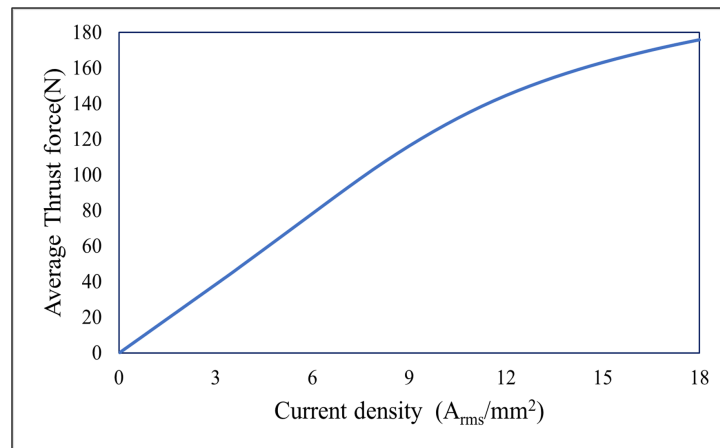
Figure 22. Average thrust force along current density of LHEFSM.
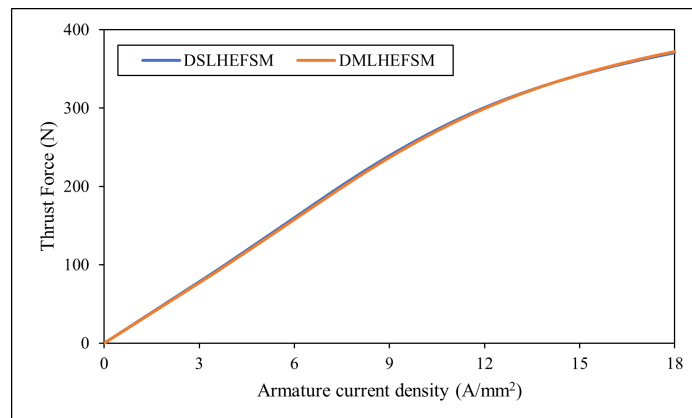
Figure 23. Average thrust force along armature current density of DSLHEFSM and DMLHEFSM.

6.6. Detent Force

The proposed machine's detent force must be determined to study noise and vibration, and it is also a significant factor in evaluating the performance of the proposed designs. The slot and end effects are combined in the detent force, a no-load force. In the no-load stage, there is simply a detent force between the iron core on the stator side and the PM on the mover side: the more robust the gravity force, the louder the vibration and noise, and the lower the output. The slot effect causes the detent force, and the primary's finite length causes the end effect. Vibrations that reoccur after a particular period of one electrical cycle make up the detent force. The end detent component should be eliminated to reduce noise and improve machine performance. The detent force of the LHEFSM varied between −1 and 1, with the traditional design having a higher detent force value as shown in Figure 24. The range of fluctuation of the detent force was 6.54 N and 2 N for the DSLHEFSM and the DMLHEFSM, respectively, which was significantly less than the typical design depicted in Figure 25.
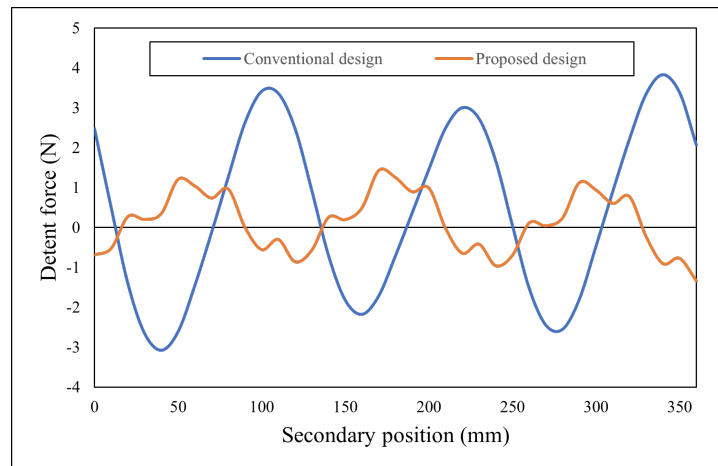
**Figure 24.** Detent force of LHEFSM and single-sided conventional design.
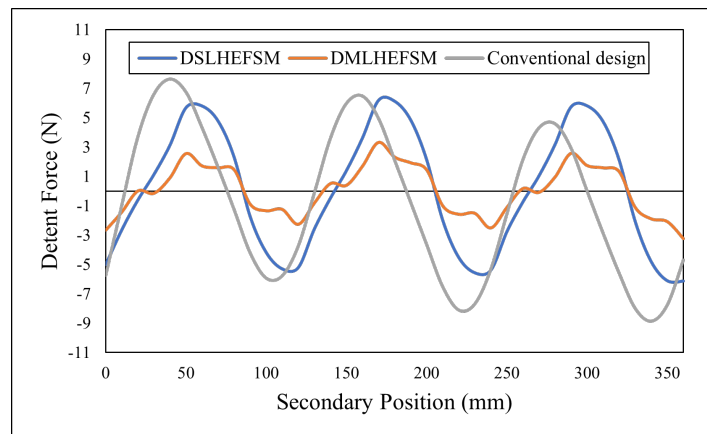
Figure 25. Detent force characteristics of DSLHEFSM, DMLHEFSM, and conventional design.

6.7. Normal Force

The restoring force is thought to maintain the vehicle in the intended position at all times in order to avoid side interference. The normal force always acts outward and is perpendicular to the contact surface. The asymmetric air gap distribution causes the normal force of the double-sided model. Because the symmetrical air gaps negate each other's impact, the net normal force of the double-sided machine is close to zero. The normal force had a more substantial effect on the vibration than the detent force [31]. The DSLHEFSM normal force is illustrated in Figure 26; when the displacement in the X direction varied, the normal force fluctuated with a fluctuation range of 0.18 N and an average normal force of 0.0056 N. The DMLHEFSM had a lower normal force value, however it was high before optimization, as illustrated in Figure 27.
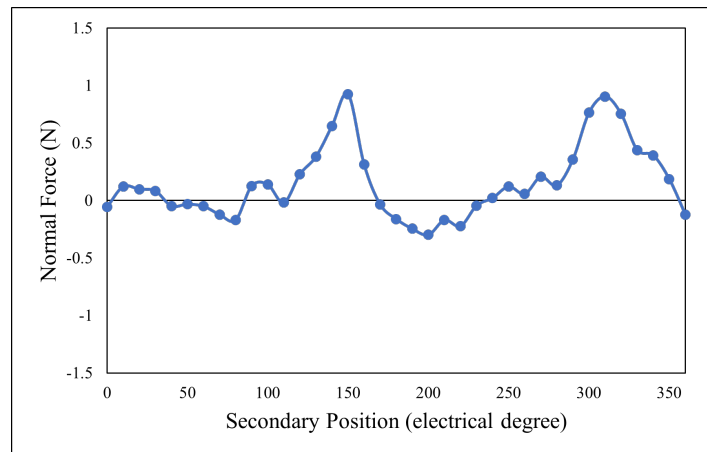
Figure 26. Normal force of DSLHEFSM.
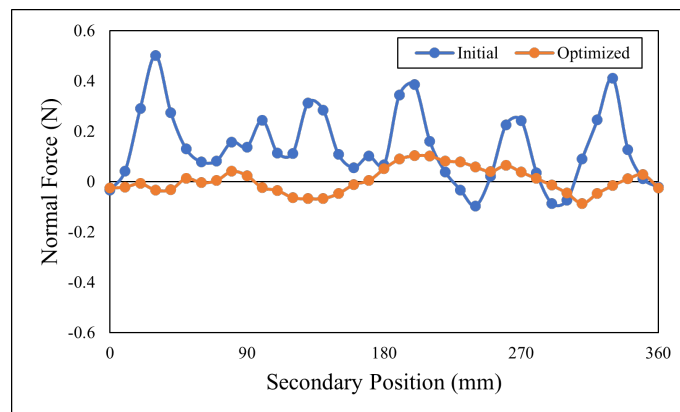
Figure 27. Normal force of DMLHEFSM.

6.8. 3D Analysis

Three-dimensional FEA was used to validate the 2D FEA results and illustrate the lateral effect. The flux linkage estimated by 2D and 3D FEA is addressed in Figures 28–30 for the LHEFSM, the DSLHEFSM, and the DMLHEFSM, respectively. The waveforms of the 2D and 3D findings appear to be rather closely matched. The thrust force in 2D and 3D is also compared in Figures 31–33, and the results are well coordinated. The difference is not significant, but the thrust force in 3D was lowered owing to longitudinal end effects. When compared to a 2D construction, the average thrust force was reduced by almost 5.6 percent. The thrust ripple rate of 3D was higher than 2D due to the end effects. For both double-sided constructions, the normal force was determined. The 3D normal force for the DSLHEFSM and the DMLHEFSM is depicted in Figure 34 and Figure 35, respectively. Because of the 3D impact, the normal force in 3D analysis is substantially higher than in 2D analysis.
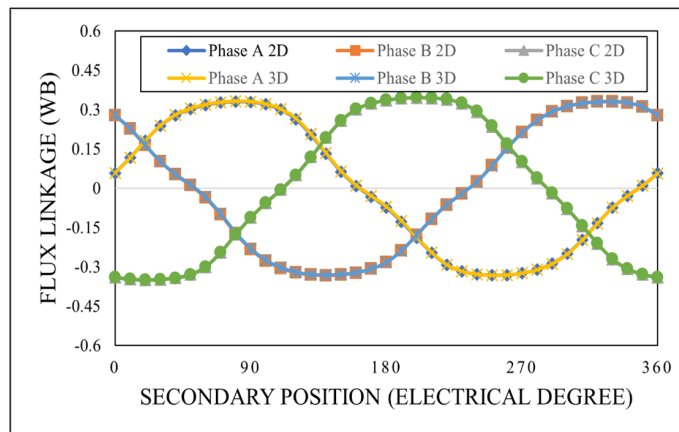
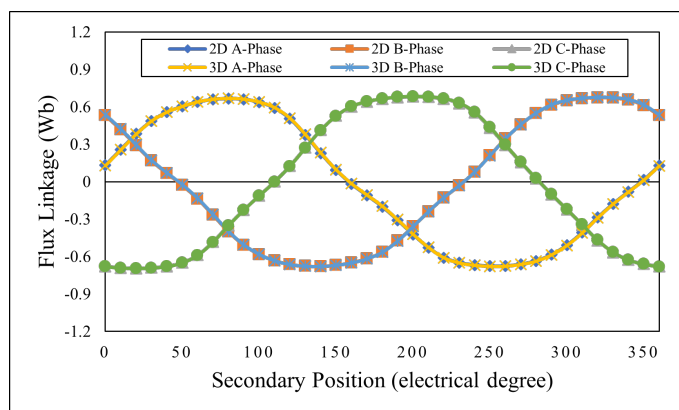**Figure 28.** Comparison of 2D and 3D flux linkage, proposed LHEFSM.

Figure 29. Comparison of 2D and 3D FE flux linkages, proposed DSLHEFSM.
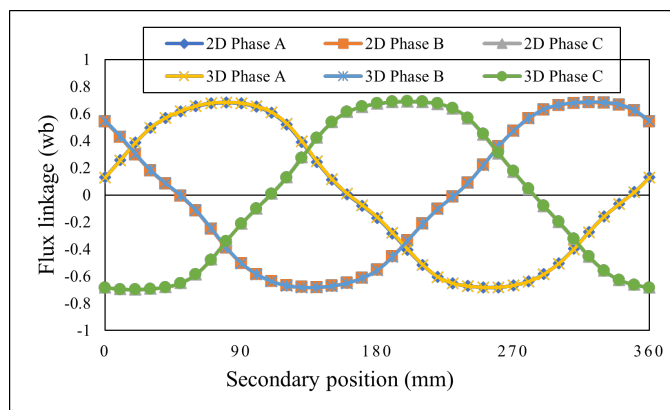

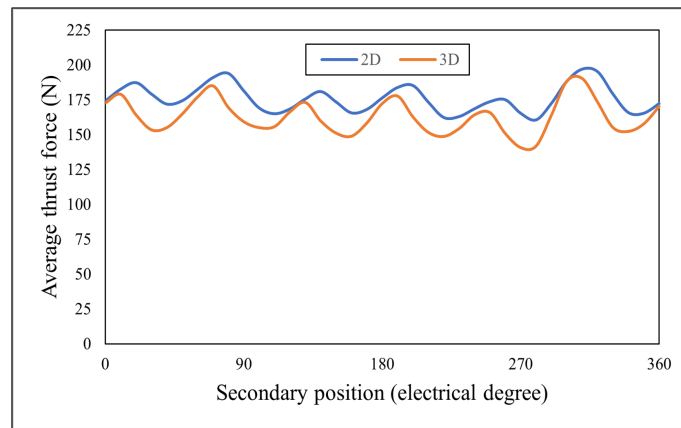**Figure 30.** Comparison of 2D and 3D FE flux linkages, proposed DMLHEFSM.

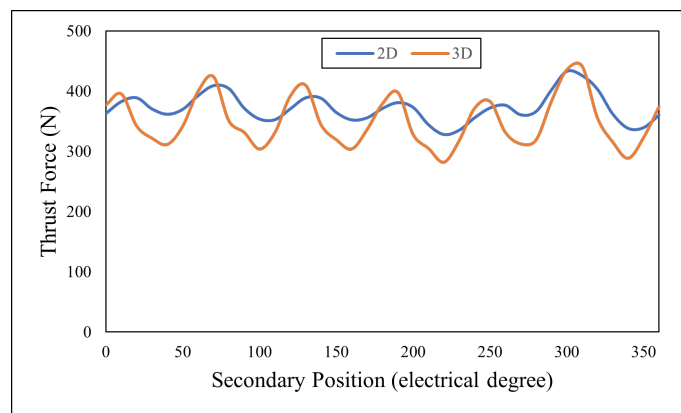**Figure 31.** Comparison of 2D and 3D thrust force, proposed LHEFSM.

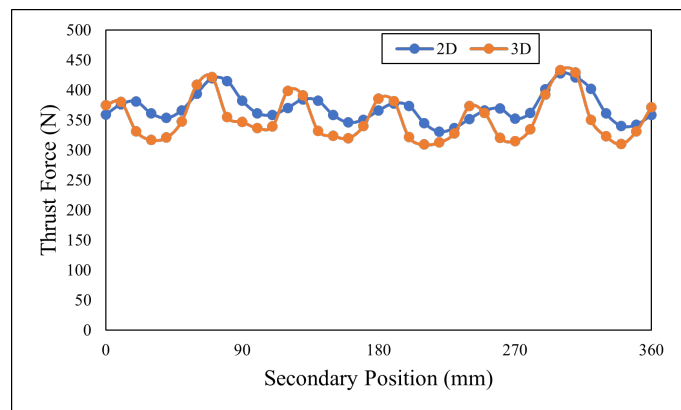**Figure 32.** Comparison of 2D and 3D average thrust force, proposed DSLHEFSM.

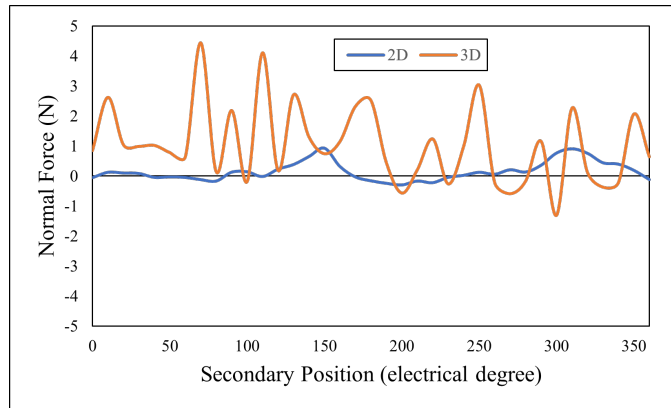**Figure 33.** Comparison of 2D and 3D average thrust force, proposed DMLHEFSM.

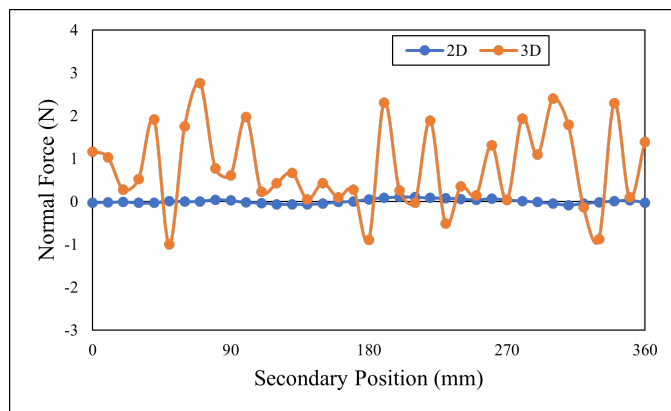**Figure 34.** Comparison of 2D and 3D normal force, proposed DSLHEFSM.

Figure 35. Comparison of 2D and 3D normal force, proposed DMLHEFSM.

6.9. Magnetic Flux Density

When the primary is in the starting position, the motor's 3D magnetic flux density nephogram is depicted in Figures 36–38. The magnetic flux density was concentrated primarily on the primary core at the teeth location, where the armature and DC coil come into contact. The material's highest magnetic field was 2.2 T, which is significantly higher than the primary's maximum field of 1.8 T. The increased magnetic field density in the primary core's center, which did not surpass 1.8 T, implies minimal magnetic saturation.
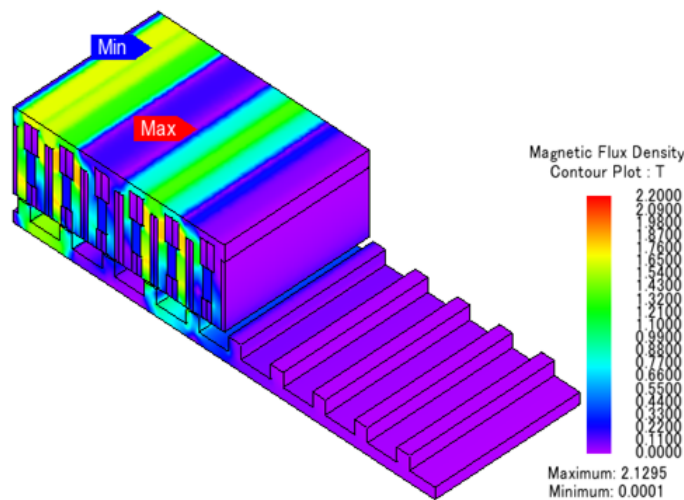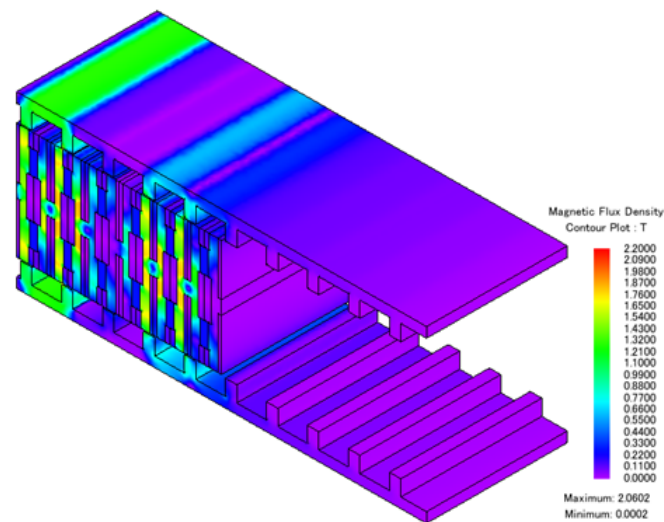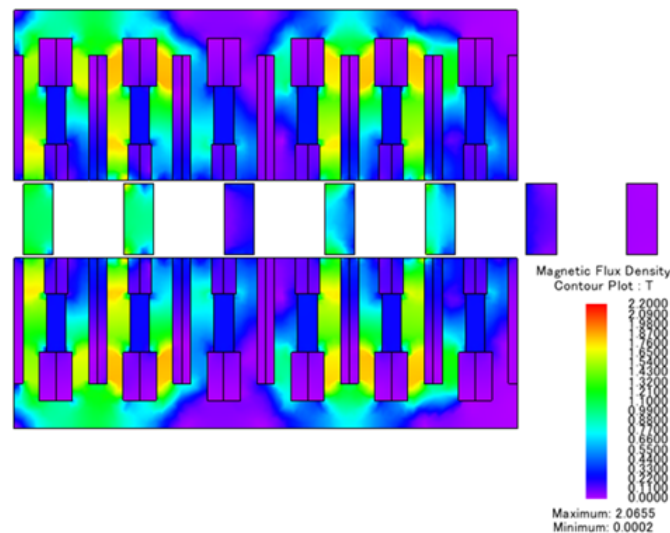

Figure 36. Magnetic flux density of LHEFSM.

Figure 37. Magnetic flux density of DSLHEFSM.

Figure 38. Magnetic flux density of DMLHEFSM.

6.10. Force-Speed Characteristics

Machines frequently require force-speed characteristics in order to accomplish effective position control. Using the approach described in [32], the force-velocity and output power–velocity curves was produced. For the LHEFSM, the force–velocity curve and the power–velocity curves at the pole pitch periodic boundary are presented in Figure 39, indicating that the machine was employed for variable speed and had limited constant power control. As illustrated in Figures 40 and 41, both double-sided designs exhibited almost identical force and power graphs.
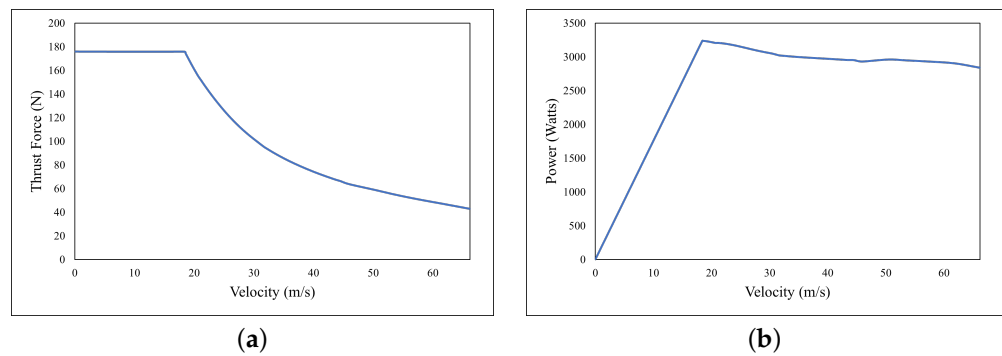
Figure 39. Characteristics of LHEFSM: (**a**) force velocity and (**b**) power velocity.
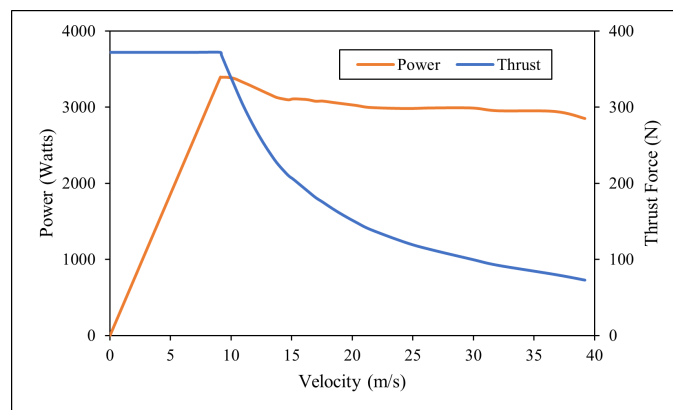

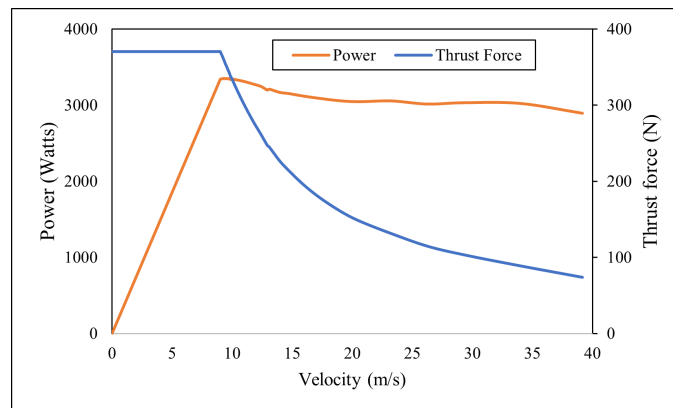**Figure 40.** Force/power velocity characteristics of DSLHEFSM.

Figure 41. Force/power velocity characteristics of DMLHEFSM.

6.11. Efficiency

The linear machine's output power was computed as the direct product of the thrust force and the linear velocity, while the input power was calculated as the sum of the output power and the total losses. Under the force velocity graph, the losses were estimated at 12 different points with the changing velocity and the electric loading. In Figure 42, the average effectiveness of 12 points was 83 percent of the LHEFSM. For the DSLHEFSM, the losses were estimated at 19 distinct places on the force–velocity graph with varied velocity and electric loading, as shown in Figure 43. P1 was taken at a maximum electric loading and a velocity of 9.11 m/s, with 628 and 621 watts of copper and iron loss, respectively. At a maximum velocity of 39 m/s, the point P19 had a maximum iron loss of 1398 watts. As indicated in Figure 44, the average effectiveness of 19 points was 76 percent. The losses for DMLHEFSM were calculated using a changing velocity and electric loading beneath the force–velocity graph at 14 different locations. Copper and iron losses are proportional

to electric loads and velocity. Copper losses include the coil's end winding as well. Iron losses were calculated using 2D FEA. At the maximal electric loading and velocity of 9 m/s, point P1 was taken with the copper 621 watts. P14 had a maximum iron loss of 501 watts at a velocity of 39 m/s. A total of 14 points were extracted from the force–velocity curve. As seen in Figure 45, 14 points had a 76 percent average efficiency.
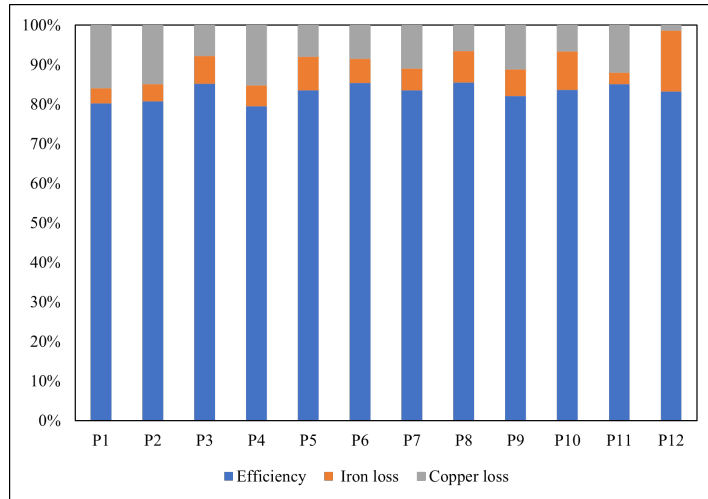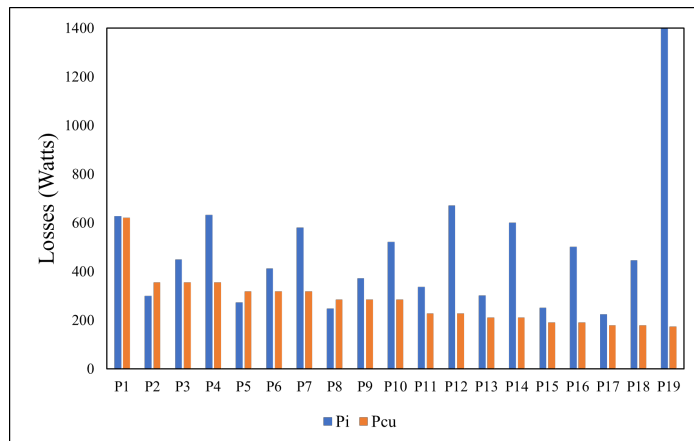

Figure 42. Efficiency at 12 points, LHEFSM.

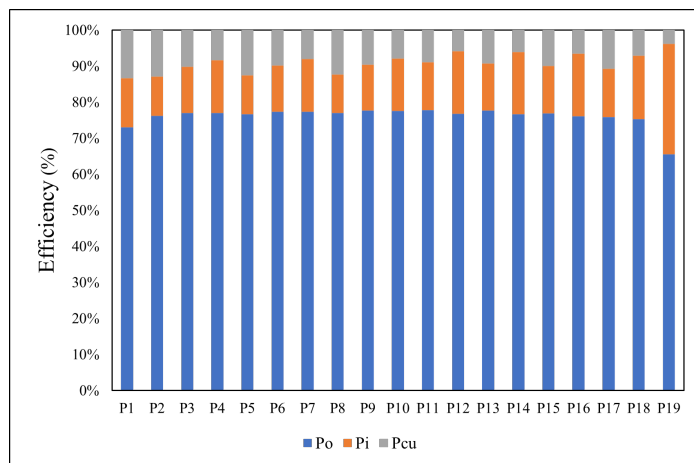**Figure 43.** Copper and iron losses at 19 different points, proposed DSLHEFSM.

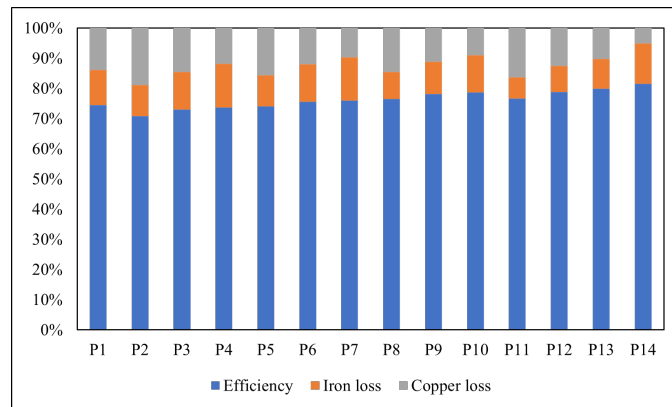**Figure 44.** Efficiency graph at 19 different points, proposed DSLHEFSM.

Figure 45. Efficiency graph at 14 different points, proposed DMLHEFSM.

6.12. Thermal Analysis

A magnetic field analysis based on the finite element method must correctly deal with the iron cores, the iron loss, and the magnet's eddy current. In the thermal analysis, we dealt with the motor's heat transmission problem. The temperature distribution was determined using thermal analysis based on the calorific value of the magnetic field study. The heat created by these losses will be transported to the interior of the motor construction, causing each motor section to heat up. Figure 46 depicts the temperature distribution.
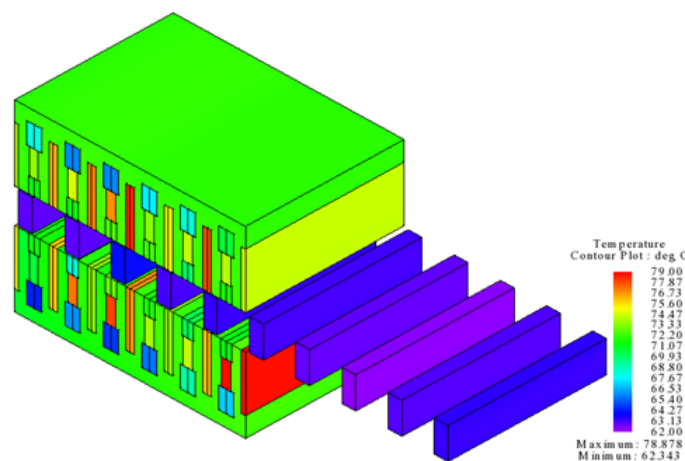
Figure 46. Thermal analysis of DMLHEFSM.

6.13. Comparison with Conventional Model

Finally, the presented designs were compared with the conventional designs proposed in the literature, and the detailed comparison is given in Table 8.

Table 8. Comparison of proposed and conventional designs.

Parameter	LHEFSM	[29]	DSLHEFSM	DMLHEFSM	[30]
Mover Length	131 mm			131 mm	
Stack Length	90 mm			90 mm	
Air gap	0.8 mm			0.8 mm	
Field Density			8 A/mm^2		
PM Volume	44.32 cm^3	55.4 cm^3		88.64 cm^3	110.8 cm^3
Thrust Force	175.93 N	152.53 N	372 N	370 N	312.8 N

7. Conclusions

The LHEFSM, the DSLHEFSM, and the DMLHEFSM were suggested in this study. In comparison to conventional designs, the suggested designs have greater thrust force, power density, and decreased normal force while reducing the volume of permanent magnets by 25%. A yokeless primary structure was used in DSLHEFSM to minimize the volume of the mover, which enhances thrust force density, while a yokeless secondary structure was used in the DMLHELFSM to reduce the volume of the secondary and to lower the machine's total cost. Single variable optimization was used to optimize all of the proposed designs. In comparison to traditional designs, the proposed designs had a lower normal force and a lower THD. By performing a 3D study, all of the electromagnetic performances acquired from the 2D analysis were validated. In comparison to conventional designs, the average thrust force in the LHEFSM, the DSLHEFSM, and the DMLHEFSM was enhanced by 15%, 16.8%, and 15.6%, respectively. In 2D and 3D models, the average normal force of the DSLHEFSM was 0.15 N and 1.03 N, respectively, whereas the average normal force of the DMLHEFSM was 0.0056 N and 0.76 N, respectively. High thrust density, high power density, high no-load electromotive force, and low normal force are all features of the presented machines, making them suitable for long-stroke applications. However, the presented design has the limitation of poor thermal management, which is a global issue in LFSM as all the sources are installed on the short primary. The authors aim to develop a thermal model for all of the proposed designs as a future work.

Author Contributions: Conceptualization, M.Q. and F.K.; methodology, M.Q.; software, M.Q., B.U. and H.U.J.; validation, M.Q., B.U. and H.U.J.; resources, F.K. and H.I.A.; formal analysis, B.U. and M.Q.; original draft preparation, M.Q.; visualization, B.U.; review and editing, B.U. and F.K.; supervision, F.K.; project administration, F.K. and H.I.A.; funding acquisition, H.I.A. All authors have read and agreed to the published version of the manuscript.

References

1. Magill, M. *Laboratory Experiment No. 5: Advanced Induction Machine Topics*; Royal Institute of Technology (KTH): Stockholm, Sweden, 2010.
2. Sadler, G.; Davey, A. Applications of linear induction motors in industry. *Proc. IET Inst. Electr. Eng.* **1971**, *118*, 765–776. [CrossRef]
3. Lee, H.W.; Kim, K.C.; Lee, J. Review of maglev train technologies. *IEEE Trans. Magn.* **2006**, *42*, 1917–1925.
4. Gurol, H. General atomics linear motor applications: Moving towards deployment. *Proc. IEEE* **2009**, *97*, 1864–1871. [CrossRef]
5. Roop, S.S.; Roco, C.E.; Olson, L.E.; Morgan, C.A. Freight Transportation System and Method. U.S. Patent 7,654,203, 2 February 2010.
6. Houser, M.; Price, C. Ocean Energy System and Method. U.S. Patent 7,786,609, 31 August 2010.
7. Kotlyar, O. Electrical Linear Motor for Marine Propulsion. U.S. Patent 7,604,520, 20 October 2009.
8. Yan, L.; Li, W.; Jiao, Z.; Chen, C.Y.; Chen, I.M. Design and modeling of three-phase tubular linear flux-switching permanent magnet motor. In Proceedings of the 2014 IEEE Chinese Guidance, Navigation and Control Conference, Yantai, China, 8–10 August 2014; pp. 2675–2680.
9. Zhang, B.; Cheng, M.; Cao, R.; Du, Y.; Zhang, G. Analysis of linear flux-switching permanent magnet motor using response surface methodology. *IEEE Trans. Magn.* **2014**, *50*, 1–4. [CrossRef]
10. Cao, R.; Cheng, M.; Mi, C.C.; Hua, W. Influence of leading design parameters on the force performance of a complementary and modular linear flux-switching permanent-magnet motor. *IEEE Trans. Ind. Electron.* **2013**, *61*, 2165–2175. [CrossRef]

11. Abdollahi, S.E.; Vaez-Zadeh, S. Back EMF analysis of a novel linear flux switching motor with segmented secondary. *IEEE Trans. Magn.* **2013**, *50*, 1–9. [CrossRef]

12. Khalid, S.; Khan, F.; Ahmad, Z.; Ullah, B. Design and finite element analysis of modular C-Core stator tubular linear oscillating actuator for miniature compressor. *World J. Eng.* **2021**. [CrossRef]

13. Zhu, Z.; Chen, X.; Chen, J.; Howe, D.; Dai, J. Novel linear flux-switching permanent magnet machines. In Proceedings of the 2008 International Conference on Electrical Machines and Systems, Wuhan, China, 17–20 October 2008; pp. 2948–2953.

14. Chung, S.U.; Lee, H.J.; Woo, B.C.; Kim, J.W.; Lee, J.Y.; Moon, S.R.; Hwang, S.M. A feasibility study on a new doubly salient permanent magnet linear synchronous machine. *IEEE Trans. Magn.* **2010**, *46*, 1572–1575. [CrossRef]

15. Ullah, B.; Khan, F.; Milyani, A.H.; Ahmad, N.; Cheema, K.M. Design and analysis of dual-stator hybrid excited linear flux switching machine for long-stroke applications. *IET Electr. Power Appl.* **2021**, *15*, 1678–1691. [CrossRef]

16. Ullah, B.; Khan, F.; Qasim, M.; Jan, H.U.; Khan, B.; Khalid, S. Design and Electromagnetic Performance Analysis of Linear Hybrid Excited Flux Switching Machine for Long Stroke Applications. In Proceedings of the 2021 IEEE International Power and Renewable Energy Conference (IPRECON), Kollam, India, 24–26 September 2021; pp. 1–6.

17. Ullah, B.; Khan, F.; Qasim, M.; Jan, H.U.; Khan, B.; Khalid, S. Design and Analysis of Consequent Pole Dual Stator Hybrid Excited Linear Flux Switching Machine for Rail Transit System. In Proceedings of the IEEE 2021 International Conference on Emerging Power Technologies (ICEPT), Topi, Pakistan, 10–11 April 2021; pp. 1–6.

18. Qasim, M.; Khan, F.; Jan, H.U.; Ullah, B.; Ejaz, B.; Hussain, S. Novel Partitioned Primary Linear Hybrid Excited Flux Switching Machine with Segmented Secondary. In Proceedings of the IEEE 2021 International Conference on Emerging Power Technologies (ICEPT), Topi, Pakistan, 10–11 April 2021; pp. 1–6.

19. Chen, J.; Zhu, Z. Winding configurations and optimal stator and rotor pole combination of flux-switching PM brushless AC machines. *IEEE Trans. Energy Convers.* **2009**, *25*, 293–302. [CrossRef]

20. Liu, J.; Chen, Y.; Lu, Q.; Ye, Y.; Huang, X. Optimization and comparison of C-core and E-core linear switched-flux PM machines with odd primary poles. In Proceedings of the IEEE 2015 18th International Conference on Electrical Machines and Systems (ICEMS), Pattaya, Thailand, 25–28 October 2015; pp. 254–259.

21. Wang, C.; Shen, J.; Wang, L.; Wang, K. A novel permanent magnet flux-switching linear motor. In Proceedings of the 2008 4th IET Conference on Power Electronics, Machines and Drives, York, UK, 2–4 April 2008; pp. 116–119.

22. Min, W.; Chen, J.; Zhu, Z.; Zhu, Y.; Duan, G. Optimization of linear flux switching permanent magnet motor. In Proceedings of the 2010 IEEE Vehicle Power and Propulsion Conference, Lille, France, 1–3 September 2010; pp. 1–6.

23. Zheng, P.; Sui, Y.; Tong, C.; Bai, J.; Yu, B.; Lin, F. A novel single-phase flux-switching permanent magnet linear generator used for free-piston Stirling engine. *J. Appl. Phys.* **2014**, *115*, 17E711. [CrossRef]

24. Hussain, S.; Khan, F.; Ullah, W.; Ullah, B.; Khan, B. Development of a Low-Cost Modular Structure Fault Tolerant Field Excited Flux Switching Linear Machine for Urban Rail Transit. *IEEE Access* **2021**, *9*, 165854–165864. [CrossRef]

25. Zhu, Z. Switched flux permanent magnet machines—Innovation continues. In Proceedings of the IEEE 2011 International Conference on Electrical Machines and Systems, Beijing, China, 20–23 August 2011; pp. 1–10.

26. Ji, J.; Zhao, J.; Zhao, W.; Fang, Z.; Liu, G.; Du, Y. New high force density tubular permanent-magnet motor. *IEEE Trans. Appl. Supercond.* **2013**, *24*, 1–5. [CrossRef]

27. Gandhi, A.; Parsa, L. Hybrid flux-switching linear machine with fault-tolerant capability. In Proceedings of the 2015 IEEE International Electric Machines & Drives Conference (IEMDC), Coeur d'Alene, ID, USA, 11–13 May 2015; pp. 715–720.

28. Issac, S.; Poorani, S. A review on design of single sided linear induction motor to improve performance. *Int. J. Pure Appl. Math.* **2017**, *116*, 109–125.

29. Hwang, C.C.; Li, P.L.; Liu, C.T. Design and analysis of a novel hybrid excited linear flux switching permanent magnet motor. *IEEE Trans. Magn.* **2012**, *48*, 2969–2972. [CrossRef]

30. Liu, C.T.; Hwang, C.C.; Li, P.L.; Hung, S.S.; Wendling, P. Design optimization of a double-sided hybrid excited linear flux switching PM motor with low force ripple. *IEEE Trans. Magn.* **2014**, *50*, 1–4. [CrossRef]

31. Islam, M.S.; Islam, R.; Sebastian, T. Noise and vibration characteristics of permanent-magnet synchronous motors using electromagnetic and structural analyses. *IEEE Trans. Ind. Appl.* **2014**, *50*, 3214–3222. [CrossRef]

32. Qi, G.; Chen, J.; Zhu, Z.; Howe, D.; Zhou, L.; Gu, C. Influence of skew and cross-coupling on flux-weakening performance of permanent-magnet brushless AC machines. *IEEE Trans. Magn.* **2009**, *45*, 2110–2117. [CrossRef]